

Reconfigurable Intelligent Surface Assisted Spatial Modulation for Symbiotic Radio

Mingjiang Wu, Xianfu Lei, *Member, IEEE*, Xiangyun Zhou, *Senior Member, IEEE*, Yue Xiao, *Member, IEEE*, Xiaohu Tang, *Senior Member, IEEE*, and Rose Qingyang Hu, *Fellow, IEEE*

Abstract—Reconfigurable intelligent surface (RIS) is a key enabler for future paradigm-shifting communication technologies. In a cellular network, an RIS can be used to simultaneously assist the communication of a cellular link and transmit additional data for various Internet of Things (IoT) applications. This coincides with the concept of symbiotic radio (SR). In this paper, we investigate this RIS-assisted SR system. We introduce the new idea of symbiotic modulation: the modulation constellation design allows a receiver to simultaneously detect the data transmitted in the RIS-assisted cellular link and the additional IoT data transmitted by the RIS. We propose three specific modulation schemes all having the feature of receive-antenna index modulation, and hence, called symbiotic spatial modulation (SSM). The first scheme is a coherent SSM scheme with a star-QAM (quadrature amplitude modulation) constellation. Its detection performance is analyzed using either an optimal maximum likelihood detector or a suboptimal successive greedy detector. We then extend the design to two noncoherent SSM schemes and analytically derive their detection performances as well. Simulation results corroborate the analysis and illustrate good detection performance of the proposed SSM schemes for both the cellular and IoT data transmissions in the considered SR system.

Index Terms—Reconfigurable intelligent surface, symbiotic radio, symbiotic spatial modulation, star-QAM, Internet-of-Things.

I. INTRODUCTION

A. Background and Motivation

In order to develop more advanced wireless communication technologies to meet the requirements of the future digital society, the research of the sixth generation (6G) wireless communication networks has been underway. 6G will extremely enhance the Internet-of-Things (IoT) communications to enable the vision of “everything-as-a-service”, and it has been expected to support 10^7 devices/km² [1]. Massive devices and abundant communication applications would result in an explosive growth in data traffic. However, on the other hand,

the scarcity of radio spectrum, especially in sub-6 GHz, has become a key bottleneck for the development of wireless networks and the requirement of low power consumption also raises a big challenge for the network design. Consequently, there is an urgent demand for revolutionary technologies to provide spectrum- and energy-efficient solutions for 6G. In order to tackle the challenges of spectrum and power consumption, researchers have proposed ambient backscatter communication technology [2], [3], which is a novel passive technique to transmit IoT information. In ambient backscatter communication, the ambient radio frequency (RF) signal, e.g., base station (BS) or Wi-Fi signal, is utilized by ambient backscatter device as the carrier to directly modulate the IoT information in the air. Thus, RF chain is not necessary for the ambient backscatter device. Ambient backscatter communication avoids emitting new wireless signal and shares the RF signal with the RF source, leading to high spectrum and energy efficiency and low cost. However, the receiver of ambient backscatter communication always encounters the strong direct-link interference of the RF source. To deal with this problem, various interference cancellation techniques have been developed [4]–[6].

Different from the conventional ambient backscatter communication technology which considers the primary signal from the RF source as interference, the authors of [7] proposed a cooperative ambient backscatter communication system, also termed symbiotic radio (SR) [8], in which the receiver decodes information not only from the ambient backscatter device, but also from the RF source. The backscatter link generated by ambient backscatter device carries the IoT information, and simultaneously enhances the received power of primary transmission (The transmission from the RF source to its target receiver), realizing a win-win effect between the primary and passive IoT transmission. However, according to [7], the single-antenna backscatter device can only provide limited performance gain to the primary transmission due to the double path loss effect.

Recently, reconfigurable intelligent surface (RIS), which can be used to reconfigure the wireless channel, has drawn increasing attention from the research community. RIS is constituted by a large number of passive and low-cost reflecting elements, and each can impose amplitude and phase shift to the incident signal to collaboratively achieve a controllable beamforming [9]–[11]. Thanks to the massive number of reflecting elements, the spectrum and energy efficiency of RIS in communication systems are much higher than that of backscatter device, and these excellent characteristics make

M. Wu and X. Tang are with the Provincial Key Lab of Information Coding and Transmission, Southwest Jiaotong University, Chengdu, 610031, China (e-mail: mingjiang.wu@my.swjtu.edu.cn, xhutang@swjtu.edu.cn).

X. Lei is with the Provincial Key Lab of Information Coding and Transmission, Southwest Jiaotong University, Chengdu 610031, China, and also with National Mobile Communications Research Laboratory, Southeast University, Nanjing 210096, China (e-mail: xflel@swjtu.edu.cn). (*Corresponding author: Xianfu Lei*)

X. Zhou is with the School of Engineering, The Australian National University, Canberra, ACT 2601, Australia (e-mail: xiangyun.zhou@anu.edu.au).

Y. Xiao is with the National Key Laboratory of Science and Technology on Communications, University of Electronic Science and Technology of China, Chengdu 611731, China (e-mail: xiaoyue@uestc.edu.cn).

R. Q. Hu is with the Department of Electrical and Computer Engineering, Utah State University, Logan, UT 84322 USA (e-mail: rose.hu@usu.edu).

RIS is a revolutionary technology in next generation IoT networks [12]. RIS offers additional degrees of freedom to the development of wireless networks, and changes the design paradigm of wireless communication systems [13]. One of the important RIS applications is that RIS can be used as a passive transmitter to convey data, and there has been a few studies on this topic [14]–[17]. Specifically, a novel RIS-based transceiver architecture was designed in [14], in which the RIS was used as an RF chain-free transmitter and a frequency down converter for reception. Such RIS-based communication paradigms have potential superiority in the aspect of low cost, low hardware complexity, and low power consumption. Spatial modulation (SM) is a promising modulation technology in MIMO systems [18], [19], which maps the information to both the conventional two-dimensional PSK/QAM symbol and the index of transmit or/and receive antenna. Since the index of antenna is applied to carry additional information bits without extra spectrum and energy, SM has been expected to achieve high spectrum efficiency and energy efficiency by a simple design [20]. RIS also brings new opportunities for the implementation of SM. Resorting to the SM philosophy, a series of novel RIS-based modulation schemes, such as RIS-MBM (media-based modulation), RIS-SM/GSM (generalized SM), and RIS-QSM (quadrature SM), were reported in [15], and the implementation complexity and spectrum efficiency of different schemes were compared. RIS-assisted receiver-side SM were investigated in [16] and [17], where the additional information bits were transmitted by using receive-antenna index modulation. In IoT scenarios, RIS-assisted SR systems were studied in [21]–[27]. The authors of [21] utilized the ON/OFF states of the reflecting elements of RIS to modulate IoT information, and the reflecting elements being activated were used to form passive beamforming to assist the primary transmission. A low-rate IoT transmission was considered in [22]–[24], in which the binary modulation was used by the RIS to encode IoT information and simultaneously the RIS was used to assist the primary transmission through the reflective link. Multi-user MISO SR system enhanced by multiple RISs was proposed in [25], where the active beamforming at primary transmitter and the passive beamforming at each RIS were jointly optimized to maximize the weighted sum-rate of the primary and IoT transmissions. A SR system consisting of both RIS and backscatter devices was designed in [26], in which the backscatter devices were used to transmit IoT information and RIS was employed to enhance the performance of the SR system. A systematic view on SR was provided in [27], and the superiority, in terms of received power and interference cancellation, of RIS-assisted SR was emphasized.

RIS-assisted SR provides a promising solution for many application scenarios of 6G such as the smart city, smart home, and smart office. Low cost and low power consumption are very important considerations for these scenarios with massive IoT devices. In addition, RIS-assisted SR is also suitable to be adopted in electromagnetic (EM) radiation sensitive environment such as hospital and laboratory [13], since the narrow beams achieved by RIS can effectively decrease the EM interference and pollution. For future massive IoT communications, which especially concerns spectrum

efficiency, energy efficiency and hardware cost, the transceiver design is still an open challenge. Generally, the coherent detection is better than the noncoherent counterparts for error performance [28]. While the better performance of coherent detection is at the cost of high hardware and software complexity and overhead for channel state information (CSI) acquisition. The noncoherent detection does not need the CSI, and usually uses simple greedy detection, such as energy detector, to recover the transmitted information directly. Despite there is a performance gap between the noncoherent and coherent transceiver, in IoT scenarios, the noncoherent transceiver may be good enough to support some low data rate and reliability-insensitive communication tasks of IoT devices. Therefore, noncoherent transceiver would be preferred in some IoT scenarios due to its simplicity and passable bit error ratio (BER) performance. On the other hand, the recent development in the RIS gives more degrees of freedom to apply noncoherent transceiver through smartly modifying the channel coefficients [29]. One of the applications is that the RIS can cancel the channel phase to make the complex channel coefficients become real numbers, meaning that the phase modulation is suitable to be employed in the RIS-assisted noncoherent wireless communication system and the receiver can directly detect the phase information from the received signal without CSI. Moreover, the use of large number of reflecting elements can result in channel hardening, which is a typical phenomena in Massive MIMO networks [30], [31]. This property enables the amplitude modulation and its noncoherent detection to be possible, and this is one of the focuses of this paper.

B. Contributions

Different from the previous works [22]–[26], which dealt with the active and passive beamforming optimization in SR systems, this work focuses on the modulation design for RIS-assisted SR systems, where both the primary information and the additional IoT information are jointly detected at the receiver. For the first time, we propose the concept of symbiotic modulation. This new modulation approach has the “symbiotic” nature, since it jointly considers the primary information transmission and the additional IoT information transmission. The resulting modulation constellation seen by the receiver allows it to detect both streams of primary and IoT information, hence achieving the purpose of the SR system. The specific modulation schemes we design include the feature of receive-antenna index modulation. Therefore, we call the modulation schemes as symbiotic spatial modulation (SSM).

More specifically, we propose two kinds of SSM schemes, namely coherent SSM (C-SSM) scheme and noncoherent SSM (NC-SSM) scheme, to realize the coherent and noncoherent detection in the RIS-assisted SR system, respectively. For both the C-SSM and NC-SSM schemes we proposed, the receive-antenna index modulation is used by the RIS for transmitting additional IoT information. Another key characteristic of the SSM schemes is that the modulation resources (such as phase and amplitude) can be flexibly allocated to User Equipment (UE) and RIS to meet the different primary and

IoT transmission requirements, e.g., reliability and throughput, in the SR system. In the C-SSM scheme, the combined constellation symbol of UE and RIS is constructed as a star-QAM (quadrature amplitude modulation) signal. The reason for adopting star-QAM, which is a special case of circular amplitude and phase shift keying (APSK), is that the star-QAM with optimized setup can outperform the traditional PSK/QAM in SM [32]. Furthermore, the star-QAM constellation is suitable for this special signal structure of SR, since the star-QAM constellation can provide diverse and flexible solutions for the design of primary and IoT symbol sets according to the requirements of the primary and IoT transmissions such as the data rate and BER. In order to enable the noncoherent detection, the concept of NC-SSM is proposed and it consists of two different NC-SSM schemes according to the adopted different modulation techniques. For the first scheme, denoted as NC-SSM-1, we replace the star-QAM of C-SSM scheme with two PSK constellations at different amplitudes which are controlled by Manchester coding. For the second scheme, denoted as NC-SSM-2, we use PSK constellation with constant amplitude, hence there is no amplitude modulation in NC-SSM-2. We further derive the detection methods for the proposed modulation schemes and analyze the BER performance.

The rest of the paper is organized as follows. In section II, we outline the RIS-assisted SR system model. In section III, we describe the proposed C-SSM and NC-SSM schemes and their corresponding detection methods. Section IV derives the BER performance of the proposed modulation schemes and presents further optimization of the reflection parameters of the RIS. Simulation and numerical results are presented in section V to verify the effectiveness of the proposed SSM schemes, and section VI concludes the paper.

Notation: The matrix and vector are denoted by upper and lower case boldface, respectively. $[\cdot]^T$ and $[\cdot]^H$ denote transpose and conjugate transpose of a matrix or a vector. $[\cdot]_{m,n}$ represents the m -th row and the n -th column element of a matrix, and $[\cdot]_{r,:}$ represents the r -th row of a matrix. $\text{diag}(\mathbf{x})$ is the diagonal matrix, whose diagonal elements are given by the vector \mathbf{x} . \mathbf{x}_m represents the m -th element of vector \mathbf{x} . $\mathbb{C}^{x \times y}$ denotes the space of $x \times y$ complex-valued matrices. $\mathcal{CN}(\mathbf{0}, \mathbf{R})$ represents the circularly symmetric complex Gaussian distribution with zero mean and covariance matrix \mathbf{R} . \mathbf{I}_M stands for $M \times M$ identity matrix. $\|\cdot\|_2$ denotes the two norm. $(\cdot)_{\Re}/[\cdot]_{\Re}$ and $(\cdot)_{\Im}$ denote the real-part operation and the imaginary-part operation, respectively. $\mathbb{E}[\cdot]$ and $\text{D}[\cdot]$ represent expectation and variance, respectively. $\det(\cdot)$ denotes the determinant of a matrix.

II. SYSTEM MODEL

An RIS-assisted uplink SR communication system is considered, as shown in Fig. 1, which consists of a single-antenna UE, an RIS with N reconfigurable reflecting elements, IoT devices, and a BS with M antennas. The RIS associates with the IoT devices via a microcontroller, which is a field-programmable gate array (FPGA)-based component [11], [33], and is adopted to read data from the IoT devices and configure

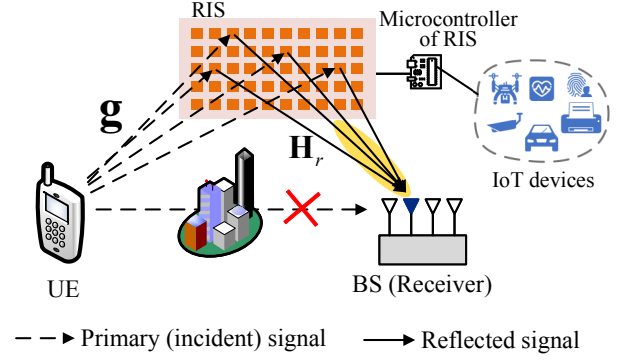


Fig. 1: RIS-assisted symbiotic radio system.

the reflection coefficients of RIS. The BS decodes the information from both the UE and IoT devices. We assume that the direct channel from the UE to the BS is blocked (i.e., absent) by obstacles, such as buildings, which is an important case in RIS-deployed scenarios [34], [35]. The RIS is employed to transmit the IoT information and meanwhile, assist the primary transmission from the UE to the BS.

Denote by $\mathbf{g} = [g_1, \dots, g_N]^T \in \mathbb{C}^{N \times 1}$ and $\mathbf{H}_r \in \mathbb{C}^{M \times N}$ the baseband equivalent channels of UE-to-RIS and RIS-to-BS, respectively. In the considered uplink system, the IoT sensors are usually close to UE so the RIS is also deployed close to UE for efficiently reflecting the primary signal from the UE while its distance to the BS is much longer. Therefore, the UE-to-RIS link is modeled as Rician fading channel in which a deterministic LoS (line of sight) component exists, while the RIS-to-BS link is modeled as Rayleigh fading channel. Specifically, \mathbf{g} with the average channel power gain σ_1^2 is given by

$$\mathbf{g} = \sigma_1 \sqrt{\frac{K_R}{K_R + 1}} \mathbf{g}^{\text{LoS}} + \sigma_1 \sqrt{\frac{1}{K_R + 1}} \mathbf{g}^{\text{NLoS}}, \quad (1)$$

where K_R is the Rician factor,

$$\mathbf{g}^{\text{LoS}} = [1, e^{j \frac{2\pi d}{\lambda_w} \sin \phi^{\text{AoA}}}, \dots, e^{j \frac{2\pi d}{\lambda_w} (N-1) \sin \phi^{\text{AoA}}}]^T \quad (2)$$

denotes the deterministic LoS path, and \mathbf{g}^{NLoS} represents the NLoS (non-LoS) path with Rayleigh distribution. In (2), d is the separation distance of reflecting elements, λ_w is the wavelength, and ϕ^{AoA} is the angle of arrival. d/λ_w can be set as 0.5 for simplicity [36]. Each element of \mathbf{g}^{NLoS} follows independent distribution of $\mathcal{CN}(0, 1)$. The above Rician channel model reduces to AWGN channel when K_R is large enough (such as larger than 30 dB) or Rayleigh channel when K_R is small enough (such as smaller than -40 dB). In addition, each element of \mathbf{H}_r follows independent distribution of $\mathcal{CN}(0, \sigma_2^2)$. Here we have $g_n = \alpha_n e^{j\varphi_n}$, which is the channel between the UE and the n -th reflecting element, and $[\mathbf{H}_r]_{m,n} = \beta_{mn} e^{j\psi_{mn}}$, which is the channel between the n -th reflecting element and the m -th receive antenna of BS, where α_n and β_{mn} are the channel amplitude, and φ_n and ψ_{mn} are the channel phase.

To facilitate receive-antenna index modulation (to be detailed in the next section), the RIS constructs M passive beam-forming vectors, which can be represented using a matrix $\Phi \in$

$\mathbb{C}^{N \times M}$, where the (n, m) -th element $[\Phi]_{n,m} = \eta_{nm}e^{j\mu_{nm}}$, and $\eta_{nm} \in [0, 1]$ and $\mu_{nm} \in [0, 2\pi)$ denote the reflection amplitude and phase shift, respectively. One of the passive beamforming vectors (i.e., one column of Φ) is used in each transmission slot. The received signal vector at the receiver (i.e., BS), $\mathbf{y} = [y_1, \dots, y_M]^T \in \mathbb{C}^{M \times 1}$, is given by

$$\mathbf{y} = \mathbf{H}\Phi\mathbf{e}^m u + \mathbf{w}, \quad (3)$$

where $\mathbf{H} = \mathbf{H}_r \text{diag}(\mathbf{g})$, and $u = x_1 x_2$. $x_1 \in \mathbb{C}$ and $x_2 \in \mathbb{C}$ are the complex-valued signals transmitted by the UE and RIS, respectively. The unit vector $\mathbf{e}^m \in \mathbb{C}^{M \times 1}$, $m \in \{1, 2, \dots, M\}$ (in which only the m -th element is 1, and the others are 0) denotes the receive-antenna index modulation signal, which means the m -th column of Φ is selected, and $\mathbf{w} = [w_1, \dots, w_M]^T \in \mathbb{C}^{M \times 1}$ is the additive white Gaussian noise vector following $\mathcal{CN}(\mathbf{0}, N_0 \mathbf{I}_M)$. By the definitions of \mathbf{H}_r and \mathbf{g} , we have $[\mathbf{H}]_{m,n} = \alpha_n \beta_{mn} e^{j(\varphi_n + \psi_{mn})}$, which denotes the cascade channel from UE to the m -th receive antenna via the n -th reflecting element of the RIS. In addition, we consider the SR scenario where x_1 and x_2 have the same symbol period. This scenario is important for IoT applications requiring high data rate.

III. PROPOSED SYMBIOTIC SPATIAL MODULATION SCHEMES AND CORRESPONDING DETECTORS

In this section, we present novel SSM schemes for both coherent detection and noncoherent detection. Their corresponding detection methods are also described.

A. Coherent Symbiotic Spatial Modulation Scheme

Firstly we present the C-SSM scheme. The constellation of the symbiotic modulation takes into account the fact that the primary signal from the UE and the IoT signal inserted by the RIS are multiplied together, i.e., $u = x_1 x_2$. In the proposed modulation scheme, we design the constellation of the combined signal u as a star-QAM. In addition, the receive-antenna index is also used to convey additional IoT information bits. Specifically, the $\log_2(K)$ primary information bits are mapped to the modulated symbol x_1 , and the $\log_2(L)$ IoT information bits are mapped to the modulated symbol x_2 which is sent by the RIS ($|x_2| \leq 1$, because the RIS cannot amplify the incident signal). Then, x_1 and x_2 are combined (through multiplication) into a (KL) -ary star-QAM symbol, i.e., u . The additional $\log_2(M)$ IoT information bits are coded into the receive-antenna index m , and the corresponding signal is \mathbf{e}^m .

We now introduce the construction of the star-QAM constellation. The construction of a general star-QAM constellation is determined by [37]: 1) the number of concentric rings; 2) the radius (amplitude) of each ring; 3) the number of constellation points of each ring and their phases. The two-ring star-QAM, where the points of each ring are evenly distributed and the phases of the points on the two rings are aligned, as shown in Fig. 2(c), is adopted in this work. The primary signal x_1 employs PSK, and the IoT signal x_2 employs two-ring APSK. Then, the combined signal u becomes a star-QAM signal by a specific design. Considering that in future wireless

networks, the IoT transmission may be dominant and the IoT services (such as video monitoring) may require high data rate, thus, the amplitude of the star-QAM is controlled by the RIS to provide higher data rate for IoT transmission. Note that the amplitude, i.e., the radius, of the star-QAM is actually the reflection amplitude of RIS, which can be controlled by adjusting the value of variable resistor embedded in each reflecting element [38].

The ratio of the radii of the two-ring star-QAM is defined as $\tau = r_2/r_1$, where r_1 and r_2 ($r_1 \leq r_2 \leq 1$, since the RIS cannot amplify the incident signal) are the inner and outer circle radius, respectively. τ needs to be optimized to minimize the BER, and the optimization process is performed in the next section. Let $x_1 = e^{j\theta_1}$ and $x_2 = \lambda e^{j\theta_2}$, $\lambda \in \{r_1, r_2\}$. Thus, $u = \lambda e^{j(\theta_1 + \theta_2)}$, and the bits carried include the one bit carried by λ (binary variable) and the remaining bits carried by the phases θ_1 and θ_2 . In the following, we develop two mapping rules to define θ_1 and θ_2 . Note that θ_2 is a $L/2$ -ary variable (i.e., it takes $L/2$ possible values) due to the two-ring structure of x_2 .

1) *Mapping Rule 1*: In this mapping rule, x_1 applies conventional K -ary PSK in the angle range of $(0, 2\pi)$, i.e., the K constellation points are uniformly distributed on a unit circle, and as a result, the θ_1 is defined as $\theta_1 = \frac{2\pi k}{K} + \kappa_0$, $k \in \{0, 1, \dots, K-1\}$, where κ_0 is the initial phase. While $e^{j\theta_2}$ applies $L/2$ -ary PSK in the angle range of $(-\pi/K, \pi/K)$, i.e., the phases of $L/2$ constellation points are uniformly distributed in $(-\pi/K, \pi/K)$, and hence the θ_2 is defined as $\theta_2 = \frac{2\pi r}{KL}$, $r \in \{\pm 1, \pm 3, \dots, \pm(\frac{L}{2} - 1)\}$. The angle range of $(-\pi/K, \pi/K)$, i.e., $2\pi/K$, equals to the phase difference of two adjacent constellation points of x_1 . Since x_1 and x_2 are multiplied together, in terms of the phase, x_1 is rotated by θ_2 , and the different phases of rotation stand for different IoT information. An example of 16-ary star-QAM with $K = 4$ and $L = 4$ under this mapping rule is shown in Fig. 2, where Fig. 2(a), 2(b), and 2(c) are corresponding to x_1 , x_2 , and u , respectively.

2) *Mapping Rule 2*: This mapping rule is realized by exchanging the definition methods of θ_1 and θ_2 in Mapping Rule 1. Specifically, $e^{j\theta_2}$ applies conventional $L/2$ -ary PSK in the angle range of $(0, 2\pi)$, i.e., $\theta_2 = \frac{4\pi r}{L} + \kappa_0$, $r \in \{0, 1, 2, \dots, L/2 - 1\}$. While x_1 applies K -ary PSK in the angle range of $(-2\pi/L, 2\pi/L)$, i.e., $\theta_1 = \frac{2\pi k}{KL}$, $k \in \{\pm 1, \pm 3, \dots, \pm(K-1)\}$, where the angle range of $(-2\pi/L, 2\pi/L)$, i.e., $4\pi/L$, equals to the phase difference of two adjacent constellation points of x_2 . An example of 16-ary star-QAM with $K = 4$ and $L = 4$ under this mapping rule is shown in Fig. 3.

According to the definitions of θ_1 and θ_2 , one can see that for the Mapping Rule 1, the error probability of detecting θ_1 is lower than that of detecting θ_2 , and the Mapping Rule 2 has the opposite result. Hence, the two mapping rules have different BER performance for the primary and IoT transmissions. Therefore, the SR system can adopt either mapping rule according to the reliability requirements. In addition, a SR system may even switch between these two mapping rules according to a certain time sharing policy. This BER-adjustable feature is suitable for the novel SR system, in

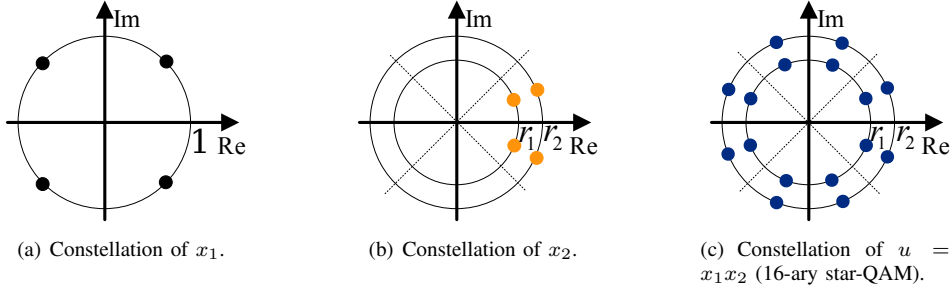


Fig. 2: Illustration of a 16-ary star-QAM with $K = 4$ and $L = 4$ under Mapping Rule 1.

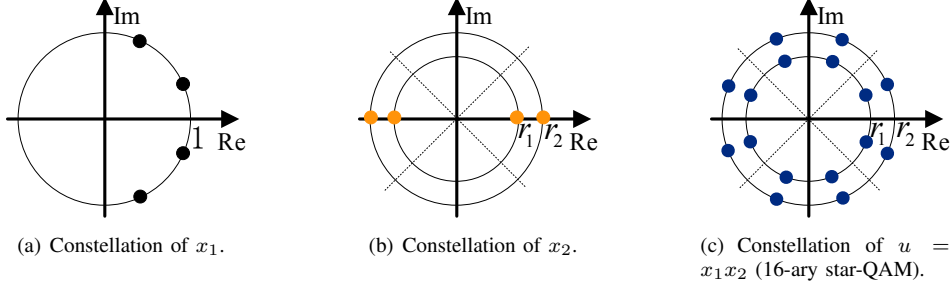


Fig. 3: Illustration of a 16-ary star-QAM with $K = 4$ and $L = 4$ under Mapping Rule 2.

which the primary and IoT transmissions may have different and dynamic reliability requirements.

The receive-antenna index modulation is realized by the RIS which adopts passive beamforming to maximize the received power at the target receive antenna [16]. Assuming the target receive-antenna index is m , and according to (3), the received signal at the m -th receive antenna, y_m , is given by

$$y_m = \sum_{n=1}^N [\mathbf{H}]_{m,n} [\Phi]_{n,m} u + w_m$$

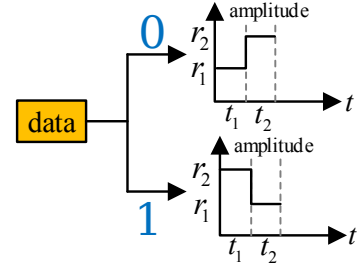
$$= u \sum_{n=1}^N \alpha_n \beta_{mn} e^{j(\varphi_n + \psi_{mn})} \eta_{nm} e^{j\mu_{nm}} + w_m. \quad (4)$$

In order to maximize $|y_m|^2$, η_{nm} should be 1 and $\mu_{nm} = -(\varphi_n + \psi_{mn})$, which means that the signals reflected by the RIS are added constructively with the same phase at the target receive antenna. Therefore, $[\Phi]_{n,m} = e^{-j(\varphi_n + \psi_{mn})}$.

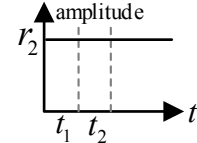
B. Noncoherent Symbiotic Spatial Modulation Schemes

Noncoherent detection is promising for future massive IoT transmission due to the low complexity. Similar to the C-SSM scheme, we have $x_1 = e^{j\theta_1}$ and $x_2 = \lambda e^{j\theta_2}$. By modifying the mapping method of λ of the C-SSM scheme, we propose two NC-SSM schemes to enable the noncoherent detection at the BS. For these two NC-SSM schemes, the PSK design, i.e., the mapping rules of θ_1 and θ_2 , and the receive antenna index modulation remain the same as the C-SSM scheme. The following descriptions are for the mapping methods of λ that differentiate the two NC-SSM schemes.

1) *NC-SSM-1*: In the NC-SSM-1 scheme, x_2 applies PSK with two different amplitudes which are decided by Manchester coding. One bit is encoded by the change in the value of



(a) NC-SSM-1: Manchester coded reflection amplitude.



(b) NC-SSM-2: Constant reflection amplitude.

Fig. 4: Reflection amplitude of the proposed noncoherent schemes.

λ in two adjacent time slots. Similarly to the C-SSM scheme, we define $\tau = r_2/r_1$, where r_1 and r_2 ($r_1 < r_2 \leq 1$) denote the low and high reflection amplitudes of the RIS, respectively. In this work, a bit “0” is encoded by the low-to-high amplitude transition, i.e., λ changes from r_1 to r_2 ; while bit “1” is encoded by the high-to-low amplitude transition, i.e., λ changes from r_2 to r_1 , as illustrated in Fig. 4(a). The optimization of τ is detailed in the next section.

2) *NC-SSM-2*: In the NC-SSM-2 scheme, the reflection amplitude is not used for information transmission any more, and x_2 applies PSK with fixed maximum reflection amplitude r_2 (as illustrated in Fig. 4(b)), i.e., $x_2 = r_2 e^{j\theta_2}$, which can maximize the received power.

TABLE I: The Comparison of The Proposed Three SSM Schemes.

SSM schemes	Amplitude and phase modulation	Index modulation
C-SSM	star-QAM	receive-antenna index modulation
NC-SSM-1	PSK and Manchester coded amplitude modulation	receive-antenna index modulation
NC-SSM-2	PSK	receive-antenna index modulation

In summary, a comparison of the proposed three SSM schemes is given in Table I.

C. Detectors Design

1) *Maximum Likelihood Detector*: We first consider the optimal ML detector for the C-SSM scheme. In ML detection, the star-QAM signal u and the receive-antenna index m are to be detected jointly. Let $\mathbf{S} = \mathbf{H}\Phi$ and $\mathbf{c} = \mathbf{e}^m u$, then (3) can be further simplified as

$$\mathbf{y} = \mathbf{S}\mathbf{c} + \mathbf{w}. \quad (5)$$

The ML detector is given by

$$(\tilde{m}, \tilde{u}) = \tilde{\mathbf{c}} = \arg \min_{\mathbf{c} \in \Gamma} \|\mathbf{y} - \mathbf{S}\mathbf{c}\|_2^2, \quad (6)$$

where Γ is the KLM -element symbol set of \mathbf{c} . According to the one-to-one mapping rules, x_1 and x_2 can be recovered after u being detected.

2) *Successive Greedy Detector*: The ML detector needs to jointly search m and u in the entire signal set Γ , which results in high computational complexity, especially when the size of Γ is large. To reduce the complexity, we consider a successive greedy (SG) detection method. The SG detector is divided into two steps. The first step is detecting the receive-antenna index using energy detection, where the receive antenna with the maximum energy of the received signal is selected. The energy detector is given by

$$\tilde{m} = \arg \max_m |y_m|^2. \quad (7)$$

The second step is to detect u based on the signal of the selected antenna. We assume m is detected correctly in the first step. The signal of m -th receive antenna is

$$y_m = \sum_{n=1}^N [\mathbf{H}]_{m,n} e^{j(-\varphi_n - \psi_{mn})} u + w_m = \sum_{n=1}^N \alpha_n \beta_{mn} u + w_m. \quad (8)$$

The constellation detector is expressed as

$$\tilde{u} = \arg \min_u \left| \frac{y_m}{\sum_{n=1}^N \alpha_n \beta_{mn}} - u \right|^2 = \arg \min_u \left| \frac{y_m}{h} - u \right|^2, \quad (9)$$

where $h = \sum_{n=1}^N \alpha_n \beta_{mn}$. As can be seen, the search space of the SG detector is $(KL + M)$, while the search space of the ML detector is (KLM) . Thus, when the modulation order is large, the computational complexity of the ML detector will be far greater than the SG detector.

3) *Noncoherent Detector*: The noncoherent detector used for NC-SSM 1 scheme consists of three steps. The first step is to detect the receive-antenna index m with the energy detector, i.e., (7). The second step is to directly detect the phase of y_m (assuming m is the detection result of the first step) without using CSI, i.e.,

$$\tilde{u} = \arg \min_u |y_m - u|^2. \quad (10)$$

In this step, u is viewed as a PSK signal, thus we only focus on the phase. The phase detection in (8) works when the receive antenna index m is correctly detected in the first step, because, in this case, h is real number (see (9)). This also means that for the phase detection, the error performance of noncoherent detector is the same as the SG detector under the correct m . The first two steps are done for each time slot. In the third (last) step, we compare the signal energy of the two selected antennas in two adjacent time slots to demodulate the Manchester coded information bit. The detection rule of the last step is defined as

$$\text{detected bit} = \begin{cases} 1, & |y_{m1}^{t1}|^2 > |y_{m2}^{t2}|^2 \\ 0, & |y_{m1}^{t1}|^2 < |y_{m2}^{t2}|^2 \end{cases}, \quad (11)$$

where y_{m1}^{t1} is the received signal of the $m1$ -th receive antenna in time slot $t1$, and a similar definition applies for y_{m2}^{t2} . $m1$ and $m2$ are the detection results of the energy detector in the adjacent slots $t1$ and $t2$, respectively.

The detection of the NC-SSM-2 scheme is simpler because it does not use amplitude in the modulation. There are only two detection steps, which are the same as the first two detection steps of the NC-SSM-1 scheme.

IV. PERFORMANCE ANALYSIS AND REFLECTION AMPLITUDE OPTIMIZATION

In this section, we focus on two aspects: 1) the theoretical BER performance of the proposed SSM schemes based on the above-mentioned detection techniques; 2) the optimization of the design parameter in the C-SSM and NC-SSM-1 schemes, that is, the ratio of the reflection amplitudes, τ .

A. Performance of C-SSM with the ML Detector

We first consider the C-SSM scheme. For mathematical tractability, we first derive the pairwise error probability (PEP) of \mathbf{c} , which will then be used to obtain an upper bound on the BER. According to (3) and (6), for a given \mathbf{S} , the PEP of \mathbf{c} is given by

$$\begin{aligned} P(\mathbf{c} \rightarrow \tilde{\mathbf{c}}) &= P(m, u \rightarrow \tilde{m}, \tilde{u}) \\ &= P(\|\mathbf{y} - \mathbf{S}\mathbf{c}\|_2^2 > \|\mathbf{y} - \mathbf{S}\tilde{\mathbf{c}}\|_2^2). \end{aligned} \quad (12)$$

Replacing \mathbf{y} with $\mathbf{S}\mathbf{c} + \mathbf{w}$, thus (12) can be rewritten as

$$P(\mathbf{c} \rightarrow \tilde{\mathbf{c}}) = P(-\|\mathbf{S}(\mathbf{c} - \tilde{\mathbf{c}})\|_2^2 - 2[\mathbf{w}^H \mathbf{S}(\mathbf{c} - \tilde{\mathbf{c}})]_{\Re} > 0) \\ = Q\left(\sqrt{\frac{\|\mathbf{S}(\mathbf{c} - \tilde{\mathbf{c}})\|_2^2}{2N_0}}\right), \quad (13)$$

where $Q(\cdot)$ is the Gaussian Q -function. By averaging over the channel coefficients, the unconditional PEP can be obtained by

$$\bar{P}(\mathbf{c} \rightarrow \tilde{\mathbf{c}}) = \int_0^\infty Q\left(\sqrt{\frac{\Delta}{2N_0}}\right) f_\Delta(\Delta) d\Delta \\ = \frac{1}{\pi} \int_0^{\frac{\pi}{2}} M_\Delta\left(\frac{-1}{4N_0 \sin^2 t}\right) dt, \quad (14)$$

where $\Delta = \|\mathbf{S}(\mathbf{c} - \tilde{\mathbf{c}})\|_2^2$, and $f_\Delta(\Delta)$ and $M_\Delta(\zeta)$ are the probability density function (PDF) and moment generating function (MGF) of Δ , respectively. In (14), the alternate representation of the Q function is used [16]. To calculate the integration in (14), we first need to calculate $M_\Delta(\zeta)$ whose derivation can be divided into two cases, depending on whether the detection of receive-antenna index is correct or incorrect. For ease of presentation, we define $\mathbf{q} = \mathbf{S}(\mathbf{c} - \tilde{\mathbf{c}})$.

1) *Case 1- Detection of Receive-Antenna Index is incorrect* ($m \neq \tilde{m}$): We let $\Delta = \Delta_1 + \Delta_2 + \Delta_3$. Δ_1 , Δ_2 , and Δ_3 are respectively defined as

$$\Delta_1 = \|\mathbf{S}_{m,m}u - \mathbf{S}_{m,\tilde{m}}\tilde{u}\|^2 \\ = \left| \sum_{n=1}^N \alpha_n \beta_{mn} \left[u - \left(e^{j(\psi_{mn} - \psi_{\tilde{m}n})} \right) \tilde{u} \right] \right|^2 \\ = |\mathbf{q}_m|^2 = (\mathbf{q}_m)_{\Re}^2 + (\mathbf{q}_m)_{\Im}^2, \quad (15)$$

$$\Delta_2 = \|\mathbf{S}_{\tilde{m},m}u - \mathbf{S}_{\tilde{m},\tilde{m}}\tilde{u}\|^2 \\ = \left| \sum_{n=1}^N \alpha_n \beta_{\tilde{m}n} \left[\left(e^{j(\psi_{\tilde{m}n} - \psi_{mn})} \right) u - \tilde{u} \right] \right|^2 \\ = |\mathbf{q}_{\tilde{m}}|^2 = (\mathbf{q}_{\tilde{m}})_{\Re}^2 + (\mathbf{q}_{\tilde{m}})_{\Im}^2, \quad (16)$$

$$\Delta_3 = \sum_{r=1(r \neq m, r \neq \tilde{m})}^M \|\mathbf{S}_{r,:}(\mathbf{e}_m u - \mathbf{e}_{\tilde{m}} \tilde{u})\|^2 \\ = \sum_{r=1(r \neq m, r \neq \tilde{m})}^M \left| \sum_{n=1}^N \alpha_n \beta_{rn} \left[e^{j(\psi_{rn} - \psi_{mn})} u - e^{j(\psi_{rn} - \psi_{\tilde{m}n})} \tilde{u} \right] \right|^2 \\ = \sum_{r=1(r \neq m, r \neq \tilde{m})}^M \left| \sum_{n=1}^N Z_{r,m,\tilde{m},n,u,\tilde{u}} \right|^2 \\ = \sum_{r=1(r \neq m, r \neq \tilde{m})}^M |\mathbf{q}_r|^2, \quad (17)$$

where $Z_{r,m,\tilde{m},n,u,\tilde{u}} = \alpha_n \beta_{rn} [e^{j(\psi_{rn} - \psi_{mn})} u - e^{j(\psi_{rn} - \psi_{\tilde{m}n})} \tilde{u}]$. α_n is independent for different n , and α_n follows Rician distribution with mean being [39]

$$E[\alpha_n] = \sigma_\alpha \sqrt{\frac{\pi}{2}} e^{-\frac{K_R}{2}} \left[(1 + K_R) I_0\left(\frac{K_R}{2}\right) + K_R I_1\left(\frac{K_R}{2}\right) \right], \quad (18)$$

and variance being

$$D[\alpha_n] = \sigma_1^2 - E^2[\alpha_n], \quad (19)$$

where $I_a(x)$ is the modified Bessel function of the first kind of order a , and $\sigma_\alpha = \sqrt{\frac{\sigma_1^2}{2K_R + 2}}$. β_{mn} , $\beta_{\tilde{m}n}$, and β_{rn} are independent and identically distributed (i.i.d) variables and follow Rayleigh distribution with mean being $\sigma_2 \sqrt{\pi}/2$ and variance being $\sigma_2^2(4 - \pi)/4$. ψ_{mn} and $\psi_{\tilde{m}n}$ are also i.i.d variables and uniformly distributed in $(-\pi, \pi)$. Thus, $(\psi_{mn} - \psi_{\tilde{m}n})$ follows a triangular distribution with $(-2\pi, 2\pi, 0)$. According to the above results, we obtain

$$E[\alpha_n \beta_{mn}] = \sigma_2 E[\alpha_n] \frac{\sqrt{\pi}}{2}, D[\alpha_n \beta_{mn}] = \sigma_1^2 \sigma_2^2 - \frac{\sigma_2^2 \pi E^2[\alpha_n]}{4}, \\ E\left[\left(\alpha_n \beta_{\tilde{m}n} e^{j(\psi_{\tilde{m}n} - \psi_{mn})}\right)_{\Re}\right] \\ = E\left[\left(\alpha_n \beta_{\tilde{m}n} e^{j(\psi_{\tilde{m}n} - \psi_{mn})}\right)_{\Im}\right] = 0, \\ D\left[\left(\alpha_n \beta_{\tilde{m}n} e^{j(\psi_{\tilde{m}n} - \psi_{mn})}\right)_{\Re}\right] \\ = D\left[\left(\alpha_n \beta_{\tilde{m}n} e^{j(\psi_{\tilde{m}n} - \psi_{mn})}\right)_{\Im}\right] = \frac{\sigma_1^2 \sigma_2^2}{2}. \quad (20)$$

Consider the likely scenario of $N \gg 1$, applying the central limit theorem (CLT), \mathbf{q}_m and $\mathbf{q}_{\tilde{m}}$ follow complex Gaussian distribution. Let $\mathbf{t} = [(\mathbf{q}_m)_{\Re}, (\mathbf{q}_m)_{\Im}, (\mathbf{q}_{\tilde{m}})_{\Re}, (\mathbf{q}_{\tilde{m}})_{\Im}]^T$, and the mean vector and covariance matrix of \mathbf{t} are

$$\mathbf{m} = [NF_1 u_{\Re}, NF_1 u_{\Im}, -NF_1 \tilde{u}_{\Re}, -NF_1 \tilde{u}_{\Im}]^T, \quad (21)$$

and

$$\mathbf{V}_c = \begin{bmatrix} \sigma_{11} & \sigma_{12} & \sigma_{13} & \sigma_{14} \\ \sigma_{12} & \sigma_{22} & \sigma_{23} & \sigma_{24} \\ \sigma_{13} & \sigma_{23} & \sigma_{33} & \sigma_{34} \\ \sigma_{14} & \sigma_{24} & \sigma_{34} & \sigma_{44} \end{bmatrix}, \quad (22)$$

respectively, where

$$\sigma_{11} = N(\sigma_1^2 \sigma_2^2 - F_1^2) u_{\Re}^2 + \frac{\sigma_1^2 \sigma_2^2 N |\tilde{u}|^2}{2}, \\ \sigma_{22} = N(\sigma_1^2 \sigma_2^2 - F_1^2) u_{\Im}^2 + \frac{\sigma_1^2 \sigma_2^2 N |\tilde{u}|^2}{2}, \\ \sigma_{33} = N(\sigma_1^2 \sigma_2^2 - F_1^2) \tilde{u}_{\Re}^2 + \frac{\sigma_1^2 \sigma_2^2 N |u|^2}{2}, \\ \sigma_{44} = N(\sigma_1^2 \sigma_2^2 - F_1^2) \tilde{u}_{\Im}^2 + \frac{\sigma_1^2 \sigma_2^2 N |u|^2}{2}, \\ \sigma_{12} = N(\sigma_1^2 \sigma_2^2 - F_1^2) u_{\Re} u_{\Im}, \sigma_{34} = N(\sigma_1^2 \sigma_2^2 - F_1^2) \tilde{u}_{\Re} \tilde{u}_{\Im}, \\ \sigma_{13} = N(F_1^2 - \frac{3}{2} F_2) \tilde{u}_{\Re} u_{\Re} + \frac{N}{2} F_2 \tilde{u}_{\Im} u_{\Im}, \\ \sigma_{14} = N(F_1^2 - \frac{3}{2} F_2) u_{\Re} \tilde{u}_{\Re} - \frac{N}{2} F_2 u_{\Im} \tilde{u}_{\Im}, \\ \sigma_{23} = N(F_1^2 - \frac{3}{2} F_2) u_{\Im} \tilde{u}_{\Im} - \frac{N}{2} F_2 u_{\Re} \tilde{u}_{\Re}, \\ \sigma_{24} = N(F_1^2 - \frac{3}{2} F_2) u_{\Im} \tilde{u}_{\Re} + \frac{N}{2} F_2 u_{\Re} \tilde{u}_{\Im}, \\ F_1 = \sigma_2 E[\alpha_n] \frac{\sqrt{\pi}}{2}, \text{ and } F_2 = \sigma_1^2 E^2[\beta_{mn}] = \frac{\sigma_1^2 \sigma_2^2 \pi}{4}. \text{ Since } \Delta_1 + \Delta_2 = \mathbf{t}^T \mathbf{A} \mathbf{t}, \text{ where } \mathbf{A} = \mathbf{I}_4, \text{ MGF of } \Delta_1 + \Delta_2 \text{ can be calculated by [16], [40, Theorem 3.2a.1]} \\ M_{\Delta_1 + \Delta_2}(\zeta) = (\det(\mathbf{I} - 2\zeta \mathbf{A} \mathbf{V}_c))^{-\frac{1}{2}} \\ \times \exp\left(-\frac{1}{2} \mathbf{m}^T [\mathbf{I} - (\mathbf{I} - 2\zeta \mathbf{A} \mathbf{V}_c)^{-1}] \mathbf{V}_c^{-1} \mathbf{m}\right). \quad (23)$$

Because of $E[(Z_{r,m,\tilde{m},n,u,\tilde{u}})_{\Re}] = E[(Z_{r,m,\tilde{m},n,u,\tilde{u}})_{\Im}] = 0$ and the independence of $Z_{r,m,\tilde{m},n,u,\tilde{u}}$ for different r ($r \neq m, r \neq \tilde{m}$), we can obtain $D[(Z_{r,m,\tilde{m},n,u,\tilde{u}})_{\Re}] = D[(Z_{r,m,\tilde{m},n,u,\tilde{u}})_{\Im}] = \sigma_1^2 \sigma_2^2 \frac{|u|^2 + |\tilde{u}|^2}{2}$. According to the CLT, Δ_3 is sum of $(M - 2)$ independent central chi-square (χ^2)

random variables with two degree-of-freedom, then we obtain the MGF of Δ_3 as

$$M_{\Delta_3}(\zeta) = \left(\frac{1}{1 - \sigma_1^2 \sigma_2^2 \zeta N (|u|^2 + |\tilde{u}|^2)} \right)^{M-2}. \quad (24)$$

Therefore, the MGF of Δ can be obtained by

$$M_{\Delta}(\zeta) = M_{(\Delta_1 + \Delta_2) + \Delta_3}(\zeta) = M_{\Delta_1 + \Delta_2}(\zeta) M_{\Delta_3}(\zeta). \quad (25)$$

2) *Case 2- Detection of Receive-Antenna Index is Correct* ($m = \tilde{m}$): Similarly, we write Δ as $\Delta = \Delta_1 + \Delta_2$, where

$$\Delta_1 = \left| \sum_{n=1}^N \alpha_n \beta_{mn} (u - \tilde{u}) \right|^2 = |\mathbf{q}_m|^2, \quad (26)$$

$$\begin{aligned} \Delta_2 &= \sum_{r=1(r \neq m)}^M \left| \sum_{n=1}^N \alpha_n \beta_{rn} e^{j(\psi_{rn} - \psi_{mn})} (u - \tilde{u}) \right|^2 \\ &= \sum_{r=1(r \neq m)}^M |\mathbf{q}_r|^2. \end{aligned} \quad (27)$$

The MGFs $M_{\Delta_1}(\zeta)$ and $M_{\Delta_2}(\zeta)$ can be obtained by applying the same procedures as for $M_{\Delta_1 + \Delta_2}(\zeta)$ and $M_{\Delta_3}(\zeta)$ in Case 1. Thus,

$$M_{\Delta}(\zeta) = M_{\Delta_1}(\zeta) M_{\Delta_2}(\zeta). \quad (28)$$

Now we have obtained the expression of $M_{\Delta}(\zeta)$ in both cases. Substituting either (25) or (28) into (14) and performing the integration, the PEP of (14) can be obtained. According to the obtained PEP, an upper bound of BER of ML detector is given by

$$P_{C-SSM}^{ML} \leq \frac{1}{MKL} \sum_m \sum_{\tilde{m}} \sum_u \sum_{\tilde{u}} \frac{\bar{P}(\mathbf{c} \rightarrow \tilde{\mathbf{c}}) e(\mathbf{c} \rightarrow \tilde{\mathbf{c}})}{\log_2(MKL)}, \quad (29)$$

where $e(\mathbf{c} \rightarrow \tilde{\mathbf{c}})$ is the number of bit errors for \mathbf{c} being detected as $\tilde{\mathbf{c}}$. According to the mapping rule between \mathbf{c} and the primary and IoT information bits, the BER bounds of primary and IoT information bits under the ML detector are given by

$$P_{primary}^{ML} \leq \frac{1}{MKL} \sum_m \sum_{\tilde{m}} \sum_u \sum_{\tilde{u}} \frac{\bar{P}(\mathbf{c} \rightarrow \tilde{\mathbf{c}}) e(x_1 \rightarrow \tilde{x}_1)}{\log_2(K)}, \quad (30)$$

and

$$\begin{aligned} P_{IoT}^{ML} &\leq \frac{1}{MKL} \sum_m \sum_{\tilde{m}} \sum_u \sum_{\tilde{u}} \frac{\bar{P}(\mathbf{c} \rightarrow \tilde{\mathbf{c}}) e[(x_2, m) \rightarrow (\tilde{x}_2, \tilde{m})]}{\log_2(ML)}, \end{aligned} \quad (31)$$

respectively, where the definitions of $e(x_1 \rightarrow \tilde{x}_1)$ and $e[(x_2, m) \rightarrow (\tilde{x}_2, \tilde{m})]$ are similar to that of $e(\mathbf{c} \rightarrow \tilde{\mathbf{c}})$.

B. Performance of C-SSM with the SG Detector

Now we obtain an BER expression for the SG detector. For mathematical tractability, we use the following expression,

$$P^{SG} = 0.5P_e + [1 - P_e]P, \quad (32)$$

to approximate the exact BER, where P_e stands for the probability of incorrectly detecting the receive-antenna index, and P stands for the BER of detection on u given the receive-antenna index is correctly detected. The approximation in (32) uses the assumption that the BER of detection on u is 0.5 when the receive-antenna index is incorrectly detected. The PEP-based bound on P_e is

$$P_e \leq \sum_{\tilde{m}=1, \tilde{m} \neq m}^M \bar{P}(m \rightarrow \tilde{m}) = (M-1)\bar{P}(m \rightarrow \tilde{m}), \quad (33)$$

where $\bar{P}(m \rightarrow \tilde{m})$ is the average PEP of the receive-antenna index over all u , and it can be obtained by

$$\bar{P}(m \rightarrow \tilde{m}) = \frac{1}{KL} \sum_u P(m \rightarrow \tilde{m}|u). \quad (34)$$

The term $P(m \rightarrow \tilde{m}|u)$ is calculated by the following steps

$$\begin{aligned} P(m \rightarrow \tilde{m}|u) &= P(|y_m|^2 < |y_{\tilde{m}}|^2 | u) \\ &= P\left(\left|\sum_{n=1}^N \alpha_n \beta_{mn} u + w_m\right|^2 < \left|\sum_{n=1}^N \alpha_n \beta_{\tilde{m}n} e^{j(\psi_{\tilde{m}n} - \psi_{mn})} u + w_{\tilde{m}}\right|^2\right) \\ &= P\left(|hu + w_m|^2 < |\hat{h}u + w_{\tilde{m}}|^2\right), \end{aligned} \quad (35)$$

where $\hat{h} = \sum_{n=1}^N \alpha_n \beta_{\tilde{m}n} e^{j(\psi_{\tilde{m}n} - \psi_{mn})}$. According to (20), the mean and variance of h are $E[h] = NF_1$ and $D[h] = N(\sigma_1^2 \sigma_2^2 - \frac{\sigma_2^2 \pi E^2[\alpha_n]}{4})$, respectively. Similarly, $E[\left(\hat{h}\right)_{\Im}] = E[\left(\hat{h}\right)_{\Re}] = 0$ and $D[\left(\hat{h}\right)_{\Im}] = D[\left(\hat{h}\right)_{\Re}] = \sigma_1^2 \sigma_2^2 \frac{N}{2}$. We rewrite $\bar{P}(m \rightarrow \tilde{m}|u)$ as

$$P(m \rightarrow \tilde{m}|u) = P(\rho_1^2 + \rho_2^2 - \rho_3^2 - \rho_4^2 < 0), \quad (36)$$

where $\rho_1 = (hu + w_m)_{\Re}$, $\rho_2 = (hu + w_m)_{\Im}$, $\rho_3 = (\hat{h}u + w_{\tilde{m}})_{\Re}$ and $\rho_4 = (\hat{h}u + w_{\tilde{m}})_{\Im}$. We define $\rho = \rho_1^2 + \rho_2^2 - \rho_3^2 - \rho_4^2 = \mathbf{t}^T \mathbf{A} \mathbf{t}$, where $\mathbf{t} = [\rho_1, \rho_2, \rho_3, \rho_4]^T$ and $\mathbf{A} = \text{diag}([1, 1, -1, -1]^T)$. Thus, the mean vector and covariance matrix of \mathbf{t} can be obtained in the same manner as done in Case 1 of the ML detection, and then the MGF of ρ , $M_{\rho}(\zeta)$, can also be calculated through (23). The characteristic function of ρ , $\Theta_{\rho}(\omega)$, can be obtained by $\Theta_{\rho}(\omega) = M_{\rho}(j\omega)$. The cumulative distribution function (CDF) $P(\rho \leq z)$ is given by [16]

$$P(\rho \leq z) = \frac{1}{2} - \int_0^{\infty} \frac{(e^{-j\omega z} \Theta_{\rho}(\omega))_{\Im}}{\omega \pi} d\omega. \quad (37)$$

Thus, $P(m \rightarrow \tilde{m}|u)$ can be obtained by setting $z = 0$, and finally (33) can be solved. In the following, we derive the PEP of u under the assumption of correct detection of m . According to (9), the PEP is

$$P(u \rightarrow \tilde{u}) = P\left(\left|\frac{y_m}{h} - u\right|^2 > \left|\frac{y_{\tilde{m}}}{h} - \tilde{u}\right|^2\right). \quad (38)$$

Following similar steps as in Case 2 of the ML detection, the unconditional PEP of (38), i.e., $\bar{P}(u \rightarrow \tilde{u})$, can be obtained. Then the BER of u is

$$P = \frac{1}{KL} \sum_u \sum_{\tilde{u}} \frac{\bar{P}(u \rightarrow \tilde{u})e(u \rightarrow \tilde{u})}{\log_2(KL)}, \quad (39)$$

where $e(u \rightarrow \tilde{u})$ is the number of bit errors for u being detected as \tilde{u} . Therefore, substituting (33) and (39) into (32), the BER of the C-SSM scheme with the SG detector can be obtained. Furthermore, analogous to (30) and (31), and according to (39), the BER of x_1 and x_2 with the SG detector are

$$P_{x_1}^{SG} = \frac{1}{KL} \sum_u \sum_{\tilde{u}} \frac{\bar{P}(u \rightarrow \tilde{u})e(x_1 \rightarrow \tilde{x}_1)}{\log_2(K)}, \quad (40)$$

and

$$P_{x_2}^{SG} = \frac{1}{KL} \sum_u \sum_{\tilde{u}} \frac{\bar{P}(u \rightarrow \tilde{u})e(x_2 \rightarrow \tilde{x}_2)}{\log_2(L)}, \quad (41)$$

respectively. As a result, according to (32), the BER of primary and IoT information bits with the SG detector, denoted by $P_{primary}^{SG}$ and P_{IoT}^{SG} , respectively, can be separately obtained by substituting the term P in (32) with $P_{x_1}^{SG}$ and $P_{x_2}^{SG}$.

C. Performance of NC-SSM

Now we turn our attention to the NC-SSM schemes and obtain the BER performance. We first derive the BER of the NC-SSM-1 scheme with noncoherent detector. In order to simplify the derivation, it is assumed that the receive-antenna index has been detected correctly in every time slot, which is a reasonable assumption under the medium and high signal-to-noise ratio (SNR) regimes since the detection error is dominated by the incorrect detection on u rather than m in these regimes. Therefore, for the noncoherent detector, the error events include the errors of phase detection and energy comparison, which are corresponding to Step 2 and Step 3 of the noncoherent detection, respectively. For the phase detection (i.e., Step 2) of the NC-SSM-1 scheme, x_2 is viewed as a L -ary PSK signal. For the PSK signal u , the PEP is

$$P(u \rightarrow \tilde{u}) = P(|y_m - u|^2 > |y_m - \tilde{u}|^2). \quad (42)$$

Thus, the BER of x_1 and x_2 in the NC-SSM-1 scheme, respectively denoted by $P_{x_1}^{NC-SSM}$ and $P_{x_2}^{NC-SSM}$, can be calculated by the same methods as (38)-(41). As mentioned in the previous section, the BS demodulates the Manchester coded information by detecting the transition of signal energy in two adjacent time slots. Without loss of generality, assuming that in t_1 and t_2 , the employed reflection amplitude is r_2 and r_1 , respectively. Thus, according to (11), the error probability of signal energy comparison is given by

$$\begin{aligned} P_{MC} &= P(|y_{m1}^{t1}|^2 < |y_{m2}^{t2}|^2) \\ &= P(|h_{m1}^{t1}u_{r2} + w_{m1}^{t1}|^2 < |h_{m2}^{t2}u_{r1} + w_{m2}^{t2}|^2), \end{aligned} \quad (43)$$

where h_{m1}^{t1} , u_{r2} , and w_{m1}^{t1} denote the channel (real value) from the UE to the $m1$ -th receive antenna via RIS, the combined signal u with RIS applying a reflection amplitude of r_2 , and the noise of the $m1$ -th receive antenna at t_1 slot, respectively, and

similar definitions are for h_{m2}^{t2} , u_{r1} , and w_{m2}^{t2} . Expression (43) has the similar form as (35), thus, adopting the same analytical method as the energy detector for the C-SSM scheme with the SG detector, an expression of P_{MC} can be obtained. As a result, the BER of IoT information bits is

$$P_{IoT}^{NC} = \frac{\log_2(L) P_{x_2}^{NC-SSM} + 0.5 P_{MC}}{\log_2(ML) + 0.5}. \quad (44)$$

Since two time slots are used to convey one Manchester coded information bit, on average 0.5 bit is conveyed in one time slot. Note that, $P_{x_1}^{NC-SSM}$ is the theoretical BER of primary information bits in this noncoherent detection (since the detection of receive-antenna index is assumed correct). Therefore, the overall BER of the NC-SSM-1 scheme is

$$\begin{aligned} P^{NC-SSM-1} &= \frac{P_{x_1}^{NC-SSM} \log_2(K) + P_{IoT}^{NC} [\log_2(ML) + 0.5]}{\log_2(K) + \log_2(ML) + 0.5}. \end{aligned} \quad (45)$$

In the NC-SSM-2 scheme, only the PSK signal u and receive-antenna index need to be detected. Therefore, the BER derivation of the NC-SSM-2 scheme is the same as that for the C-SSM scheme with the SG detector.

TABLE II: Optimal τ of SSM Schemes Under Different System Setups.

SSM schemes	System setup (M, N , Modulation scheme of u)	Optimal τ
C-SSM	(2, 64, 16-ary star-QAM)	1.79
	(4, 64, 16-ary star-QAM)	1.79
	(8, 64, 16-ary star-QAM)	1.79
	(2, 64, 32-star-QAM)	1.70
	(2, 128, 16-ary star-QAM)	1.79
	(8, 128, 16-ary star-QAM)	1.79
NC-SSM-1	(2, 64, 32-ary PSK)	1.59
	(2, 90, 32-ary PSK)	1.59
	(2, 90, 64-ary PSK)	1.41

D. Optimization of the Reflection Amplitudes

For the two-ring star-QAM in the C-SSM scheme, the modulation design has two reflection amplitudes to be optimized, i.e., the inner radius r_1 and outer radius r_2 . Clearly the optimal choice of r_2 should be the maximum possible value. We set $r_2 = 1$ as the maximum value for simplicity. Then, the remaining design is on the inner radius, which can also be captured by the ratio of the two radii, i.e., τ . The optimal τ depends on the specific star-QAM constellation, number of receive antennas, and SNR, which makes the optimization of τ analytically intractable [32]. Thus, a numerical search based on the derived BER results is a more suitable way to be adopted. According to [32] and [41], for a given setup of transceiver and RIS, the optimal τ would approach a constant value as the SNR increases. From our numerical investigations, we choose SNR = -10 dB as the condition to search the optimal τ , where the SNR is defined as $\text{SNR} = E_s/N_0$, and E_s is the energy of x_1 . We will see in the next section that -10 dB is already a relatively high SNR, and hence, suitable for the search. The upper bound on the BER under the ML detection, described by (29), is used to search for the optimal τ of the C-SSM

scheme. Table II shows the optimal τ under different system setups.

For the NC-SSM-1 scheme, the BER described by (45) is used to search for the optimal τ . The search results under different system setups are shown in Table II.

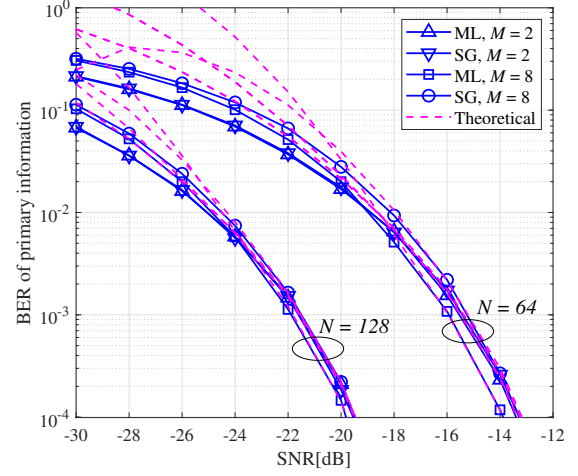
From Table II, we observe that the optimal τ highly depends on the order of constellation, because the BER under the SR detector is mainly determined by the detection performance of the constellation signal u when the SNR is sufficiently large. Additionally, it is worth mentioning that the influence of N is implied in the received SNR.

V. SIMULATION RESULTS

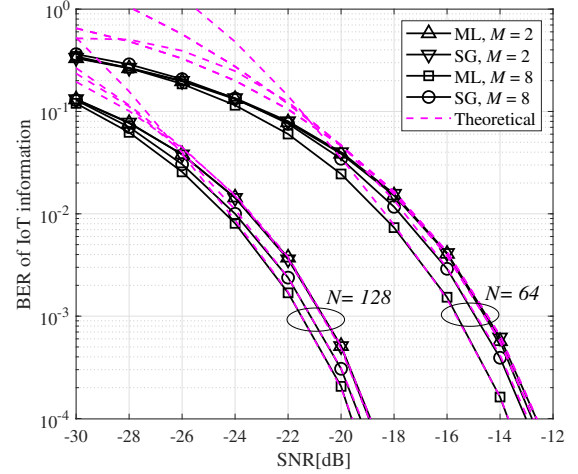
In this section, we provide simulation results to evaluate the performance of the proposed C-SSM and NC-SSM schemes. We also present results to demonstrate the impact of system parameters and choice of detectors on the system performance. For the following numerical results, the transmission of the primary information from the UE uses 4-PSK, i.e., $K = 4$. The optimal value of τ in Table II is used in all simulations. In addition, θ_1 and θ_2 of all schemes in the simulation adopt Mapping Rule 1 proposed in the C-SSM scheme, but similar conclusions are found for Mapping Rule 2 as well (the simulation results of which are not presented in this paper for brevity). For all figures, we consider the scenario where $\sigma_1 = \sigma_2 = 1$. Considering the fact that the passive IoT transmission does not have its own transmit power and shares the transmit power with the primary transmission, the transmit SNR, i.e., E_s/N_0 , can be viewed as the transmit SNR of the SR system and hence it is adopted in this section for illustrating the BER performance of both the primary and IoT transmissions.

Fig. 5 compares the BERs of the 16-ary star-QAM-aided C-SSM scheme for different M (i.e., the number of receive antennas), N (i.e., the number of RIS reflecting elements), and detectors. The Rician factor K_R is assumed to be 3 dB. We observe that all the theoretical BER curves match nicely with the simulation results in the high SNR regime, which demonstrates accuracy of the derived theoretical BER expressions. Fig. 5(a) shows the BER of the primary information. When M is 2, the ML and SG detectors have almost the same performance, while when M increases to 8, the gap between the ML and SG detectors becomes apparent, but it decreases as N increases. Overall, the BER gap between the SG and ML detectors is small (e.g., the gap less than 1 dB for $M = 8$, $N = 64$), and the reason behind this is the RIS offers powerful beamforming to activate the target receive antenna, which makes the energy detector have excellent performance. Another important observation is that increasing N can bring a significant performance gain. For instance, there is roughly 6 dB reduction for SNR at BER of 10^{-3} by increasing N from 64 to 128. In other words, a large-size RIS has significant potential for effectively increasing energy efficiency. All the above conclusions also hold in Fig. 5(b), which shows the BER performance of the IoT information.

Increasing either M or L can lead to higher IoT data rate, but it might negatively impact the BER performance. Fig. 6



(a) BER of primary information.

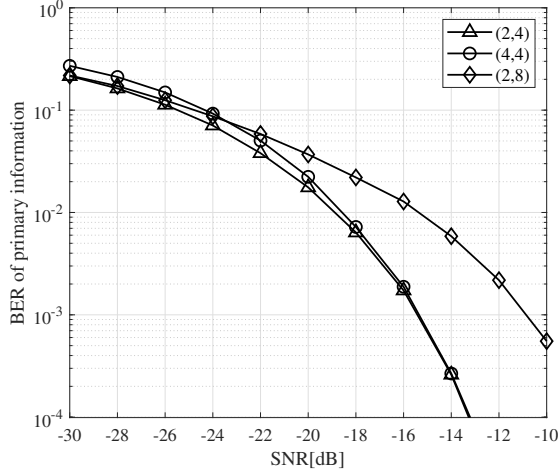


(b) BER of IoT information.

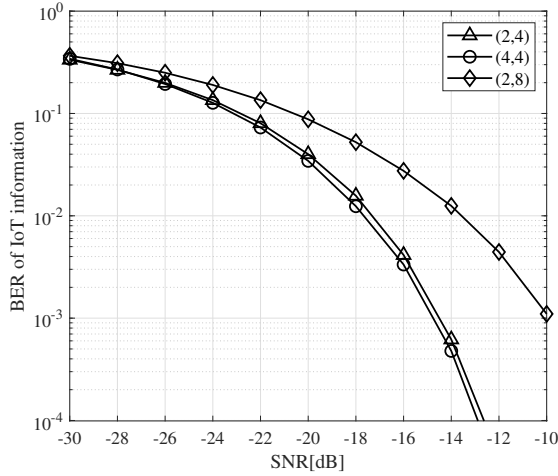
Fig. 5: BER comparison of the C-SSM scheme under the ML and SG detectors.

plots the BER of the C-SSM scheme with different combinations of (M, L) under the SG detector and $K_R = 3$ dB. We use the curve for $(2, 4)$ as the reference and compare it with the other curves to examine the impact of increasing either M or L . From Fig. 6(a) and 6(b), we can observe that in terms of the BER performance, increasing M is a good choice for improving the data rate since the BER is insensitive to the change of M . While increasing L would heavily deteriorate the BER performance. These effects imply that the receive-antenna index modulation enabled by the RIS is an excellent design choice for SSM.

To further examining the benefit of receive-antenna index modulation, Fig. 7 depicts the BER comparison between the proposed C-SSM scheme (which uses receive-antenna index modulation) with another benchmark star-QAM scheme where all receive antennas are used for signal reception under the ML detector. In this figure, $K_R = 0$ and $N = 64$. For the benchmark scheme, the lost data rate due to the absence of receive-antenna index modulation is compensated



(a) BER of primary information.

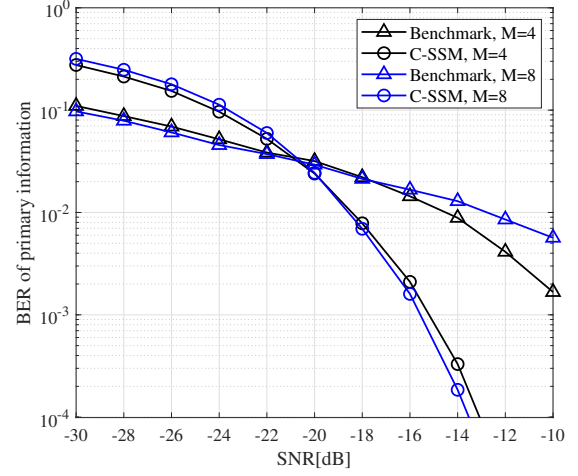


(b) BER of IoT information.

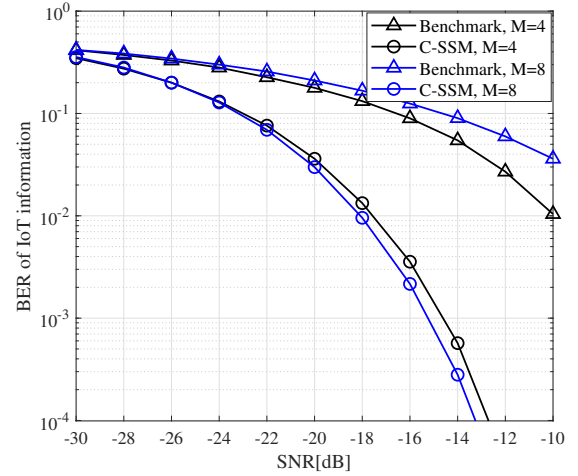
Fig. 6: BER of the C-SSM scheme for different (M, L) .

by increasing L . The optimal RIS reflecting phase shifts in the benchmark scheme are not easy to obtain, which need to be optimized using numerical algorithms. Here we adopt the alternating optimization (AO) technique to optimize the RIS reflecting phase shifts [42]. Specifically, the optimal reflecting phase shifts of all elements are alternately obtained one by one with the reflecting phase shifts of other elements being fixed. The detailed optimization process can be found in [42], [43]. Besides, the optimal ratio of the benchmark scheme's radii is numerically searched based on the simulated BER of the SR system. In Fig. 7, a 16-ary star-QAM is employed for $M = 4$ and $M = 8$ in the C-SSM scheme. To keep the same data rate with the C-SSM scheme, the constellations of the benchmark scheme with $M = 4$ and $M = 8$ employ two-ring 64-ary star-QAM and 128-ary star-QAM, respectively.

Fig. 7(a) shows the BER comparison of primary information for the two schemes. Note that although the rate of primary information transmission is the same in both schemes (i.e., K is fixed to 4 as mentioned previously), the detection performance of the primary information still depends on the



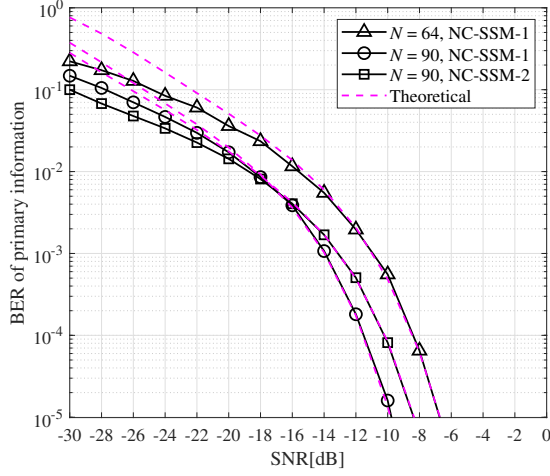
(a) BER of primary information.



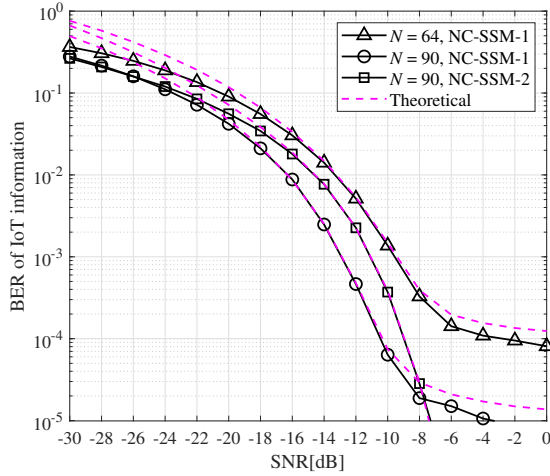
(b) BER of IoT information.

Fig. 7: BER comparison between the C-SSM scheme and benchmark scheme, $N = 64$.

overall star-QAM modulation constellation which is different for the two schemes. Firstly, it can be observed that the benchmark scheme outperforms the C-SSM scheme in the low SNR regime ($\text{SNR} < -21$ dB). This can be understood since the average reflection amplitude of the benchmark scheme is higher than that of the C-SSM scheme, which leads to higher received power (More specifically, the optimal ratios of the benchmark scheme's radii with $M = 4$ and $M = 8$ are both 1.20, while the counterparts of the C-SSM scheme are both 1.79.). While in the high SNR regime, the proposed C-SSM scheme significantly outperforms the benchmark scheme. This is because the dominant factor that influences the performance has changed from the received power to the order of the star-QAM constellation. A high constellation order heavily degrades the BER performance. Now we turn our attention to the BER of the IoT information. In addition to the difference in the star-QAM constellation, the two schemes also differ in the fact that the proposed C-SSM scheme uses receive-antenna index modulation while the benchmark scheme uses



(a) BER of primary information.



(b) BER of IoT information.

Fig. 8: BER of the NC-SSM-1 and NC-SSM-2 schemes with $M = 2$.

all receive antennas for reception. From Fig. 7(b), we see that the proposed scheme outperforms the benchmark scheme by a large margin and the performance difference increases as the SNR increases. This clearly demonstrates the advantage of using receive-antenna index modulation in the proposed SSM design.

Now we present the results for noncoherent modulation. Fig. 8 compares the BER performance of the NC-SSM-1 and NC-SSM-2 schemes under the condition of the same data rate, $M = 2$, and $K_R = 0$. We set $L = 4$ in the NC-SSM-1 scheme. On the other hand, we cannot use the same L for the NC-SSM-2 scheme, because for the same L , the Manchester coded modulation makes the NC-SSM-1 scheme convey additional 0.5 bit than the NC-SSM-2 scheme. Therefore, we use a combination of $L = 4$ and $L = 8$ in the NC-SSM-2 scheme in order to keep the same overall data rate with the NC-SSM-1 scheme. For the primary information in Fig. 8(a), with the same setting of $N = 90$, the NC-SSM-2 scheme outperforms the NC-SSM-1 scheme in the low SNR

regime, and the situation is opposite in the high SNR regime. The reason is similar to that of Fig. 7(a), i.e., the reflection amplitude is fixed at 1 in the NC-SSM-2 scheme, which is greater than the average reflection amplitude of the NC-SSM-1 scheme. Whereas in the high SNR regime, the increased received power stimulated by a high reflection amplitude cannot offset the performance loss brought by a higher order constellation.

From Fig. 8(b), it is observed that the BER of IoT information in the NC-SSM-1 scheme has an error floor in the high SNR regime, which is because the error brought by the random fluctuation of channel gain is dominant in the high SNR regime. By changing the value of N , we see that N has a significant impact on the error floor region. For instance, increasing N from 64 to 90 leads to one order-of-magnitude BER reduction in the error floor region. It can be explained as the channel hardening is more notable when increasing N . In the low to medium SNR regime, the NC-SSM-1 scheme has an advantage over the NC-SSM-2 scheme. However, the superiority of the NC-SSM-2 scheme is that it has no error floor. Therefore, for the IoT transmission in the high SNR regime, the NC-SSM-2 scheme is a better choice.

VI. CONCLUSIONS

This paper put forward the novel concept of symbiotic modulation. For the considered uplink symbiotic system with a multi-antenna BS aided by an RIS, we included the feature of receive-antenna index modulation into the design and proposed three symbiotic spatial modulation schemes with either coherent or noncoherent detection, i.e., C-SSM, NC-SSM-1 and NC-SSM-2. These modulation designs allow simultaneous transmissions of primary information and secondary IoT information both with good BER performance. For the C-SSM scheme, our results showed that the low-complexity SG detector achieves a BER performance reasonably close to that of the optimal ML detector. For the two noncoherent modulation schemes, the NC-SSM-1 scheme has superior performance in the low SNR regime while the NC-SSM-2 scheme is clearly a better choice in the high SNR regime. This paper demonstrated a great potential for using SSM or more generally symbiotic modulation to provide symbiotic communications in RIS-assisted networks. Future work could focus on new and improved designs of symbiotic modulation for better rate-reliability performance.

REFERENCES

- [1] Z. Zhang, Y. Xiao, Z. Ma, M. Xiao, Z. Ding, X. Lei, G. K. Karagiannidis, and P. Fan, "6G wireless networks: Vision, requirements, architecture, and key technologies," *IEEE Veh. Technol. Mag.*, vol. 14, no. 3, pp. 28–41, 2019.
- [2] V. Liu, A. Parks, V. Talla, S. Gollakota, D. Wetherall, and J. R. Smith, "Ambient backscatter: Wireless communication out of thin air," *ACM SIGCOMM Comput. Commun. Rev.*, vol. 43, no. 4, pp. 39–50, Oct. 2013.
- [3] N. Van Huynh, D. T. Hoang, X. Lu, D. Niyato, P. Wang, and D. I. Kim, "Ambient backscatter communications: A contemporary survey," *IEEE Commun. Surveys Tuts.*, vol. 20, no. 4, pp. 2889–2922, 4th Quart., 2018.
- [4] D. Bharadia, K. R. Joshi, M. Kotaru, and S. Katti, "Backfi: High throughput wifi backscatter," *ACM SIGCOMM Comput. Commun. Rev.*, vol. 45, no. 4, pp. 283–296, Aug. 2015.

- [5] B. Kellogg, V. Talla, S. Gollakota, and J. R. Smith, "Passive wi-fi: Bringing low power to Wi-Fi transmissions," in *13th USENIX Symposium on Networked Systems Design and Implementation (NSDI 16)*. Santa Clara, CA: USENIX Association, mar. 2016, pp. 151–164.
- [6] G. Yang, Y.-C. Liang, R. Zhang, and Y. Pei, "Modulation in the air: Backscatter communication over ambient OFDM carrier," *IEEE Trans. Commun.*, vol. 66, no. 3, pp. 1219–1233, Mar. 2018.
- [7] G. Yang, Q. Zhang, and Y. Liang, "Cooperative ambient backscatter communications for green Internet-of-Things," *IEEE Internet Things J.*, vol. 5, no. 2, pp. 1116–1130, Apr. 2018.
- [8] R. Long, Y. Liang, H. Guo, G. Yang, and R. Zhang, "Symbiotic radio: A new communication paradigm for passive Internet of Things," *IEEE Internet Things J.*, vol. 7, no. 2, pp. 1350–1363, Feb. 2020.
- [9] M. Di Renzo, M. Debbah, D.-T. Phan-Huy, A. Zappone, M.-S. Alouini, C. Yuen, V. Sciancalepore, G. C. Alexandropoulos, J. Hoydis, H. Gacanin *et al.*, "Smart radio environments empowered by reconfigurable AI meta-surfaces: An idea whose time has come," *EURASIP J. Wireless Commun. Netw.*, vol. 2019, no. 1, pp. 1–20, May 2019.
- [10] Q. Wu and R. Zhang, "Intelligent reflecting surface enhanced wireless network via joint active and passive beamforming," *IEEE Trans. Wireless Commun.*, vol. 18, no. 11, pp. 5394–5409, Nov. 2019.
- [11] S. Gong, X. Lu, D. T. Hoang, D. Niyato, L. Shu, D. I. Kim, and Y.-C. Liang, "Toward smart wireless communications via intelligent reflecting surfaces: A contemporary survey," *IEEE Commun. Surveys Tuts.*, vol. 22, no. 4, pp. 2283–2314, 4th Quart., 2020.
- [12] L. Bariah, L. Mohjazi, S. Muhaidat, P. C. Sofotasios, G. K. Kurt, H. Yanikomeroglu, and O. A. Dobre, "A prospective look: Key enabling technologies, applications and open research topics in 6G networks," *IEEE Access*, vol. 8, pp. 174 792–174 820, 2020.
- [13] M. Di Renzo, A. Zappone, M. Debbah, M. S. Alouini, C. Yuen, J. de Rosny, and S. Tretjakov, "Smart radio environments empowered by reconfigurable intelligent surfaces: How it works, state of research, and the road ahead," *IEEE J. Sel. Areas Commun.*, vol. 38, no. 11, pp. 2450–2525, Nov. 2020.
- [14] W. Tang, M. Z. Chen, J. Y. Dai, Y. Zeng, X. Zhao, S. Jin, Q. Cheng, and T. J. Cui, "Wireless communications with programmable metasurface: New paradigms, opportunities, and challenges on transceiver design," *IEEE Wireless Commun.*, vol. 27, no. 2, pp. 180–187, Apr. 2020.
- [15] Q. Li, M. Wen, and M. Di Renzo, "Single-RF MIMO: From spatial modulation to metasurface-based modulation," *IEEE Wireless Commun.*, vol. 28, no. 4, pp. 88–95, Aug. 2021.
- [16] E. Basar, "Reconfigurable intelligent surface-based index modulation: A new beyond MIMO paradigm for 6G," *IEEE Trans. Commun.*, vol. 68, no. 5, pp. 3187–3196, May 2020.
- [17] T. Ma, Y. Xiao, X. Lei, P. Yang, X. Lei, and O. A. Dobre, "Large intelligent surface assisted wireless communications with spatial modulation and antenna selection," *IEEE J. Sel. Areas Commun.*, vol. 38, no. 11, pp. 2562–2574, Nov. 2020.
- [18] Q. Si, M. Jin, Y. Chen, N. Zhao, and X. Wang, "Performance analysis of spatial modulation aided NOMA with full-duplex relay," *IEEE Trans. Veh. Technol.*, vol. 69, no. 5, pp. 5683–5687, May 2020.
- [19] A. M. Abu-Hudrouss, M.-T. O. E. Astal, A. H. Al Habbash, and S. Aïssa, "Signed quadrature spatial modulation for MIMO systems," *IEEE Trans. Veh. Technol.*, vol. 69, no. 3, pp. 2740–2746, Mar. 2020.
- [20] M. Wen, B. Zheng, K. J. Kim, M. Di Renzo, T. A. Tsiftsis, K.-C. Chen, and N. Al-Dhahir, "A survey on spatial modulation in emerging wireless systems: Research progresses and applications," *IEEE J. Sel. Areas Commun.*, vol. 37, no. 9, pp. 1949–1972, Sep. 2019.
- [21] W. Yan, X. Yuan, and X. Kuai, "Passive beamforming and information transfer via large intelligent surface," *IEEE Wireless Commun. Lett.*, vol. 9, no. 4, pp. 533–537, Apr. 2020.
- [22] Q. Zhang, Y.-C. Liang, and H. V. Poor, "Reconfigurable intelligent surface assisted MIMO symbiotic radio networks," *IEEE Trans. Commun.*, vol. 69, no. 7, pp. 4832–4846, Jul. 2021.
- [23] Y. Ma, R. Liu, M. Li, and Q. Liu, "Passive information transmission in intelligent reflecting surface aided MISO systems," *IEEE Commun. Lett.*, vol. 24, no. 12, pp. 2951–2955, Dec. 2020.
- [24] X. Xu, Y.-C. Liang, G. Yang, and L. Zhao, "Reconfigurable intelligent surface empowered symbiotic radio over broadcasting signals," in *Proc. IEEE Glob. Commun. Conf.*, Dec. 2020, pp. 1–6.
- [25] J. Hu, Y.-C. Liang, and Y. Pei, "Reconfigurable intelligent surface enhanced multi-user MISO symbiotic radio system," *IEEE Trans. Commun.*, vol. 69, no. 4, pp. 2359–2371, Apr. 2021.
- [26] H. Chen, G. Yang, and Y.-C. Liang, "Joint active and passive beamforming for reconfigurable intelligent surface enhanced symbiotic radio system," *IEEE Wireless Commun. Lett.*, vol. 10, no. 5, pp. 1056–1060, May 2021.
- [27] Y.-C. Liang, Q. Zhang, E. G. Larsson, and G. Y. Li, "Symbiotic radio: Cognitive backscatter communications for future wireless networks," *IEEE Trans. on Cogn. Commun. Netw.*, vol. 6, no. 4, pp. 1242–1255, Dec. 2020.
- [28] S. J. Nawaz, S. K. Sharma, B. Mansoor, M. N. Patwary, and N. M. Khan, "Non-coherent and backscatter communications: Enabling ultra-massive connectivity in 6G wireless networks," *IEEE Access*, vol. 9, pp. 38 144–38 186, 2021.
- [29] S. Guo, J. Ye, P. Zhang, H. Zhang, and M.-S. Alouini, "Differential reflecting modulation for reconfigurable intelligent surface-based communications," *IEEE Commun. Lett.*, vol. 25, no. 3, pp. 907–910, Mar. 2021.
- [30] Z. Chen and E. Björnson, "Channel hardening and favorable propagation in cell-free Massive MIMO with stochastic geometry," *IEEE Trans. Commun.*, vol. 66, no. 11, pp. 5205–5219, Nov. 2018.
- [31] F. Rusek, D. Persson, B. K. Lau, E. G. Larsson, T. L. Marzetta, O. Edfors, and F. Tufvesson, "Scaling up MIMO: Opportunities and challenges with very large arrays," *IEEE Signal Process. Mag.*, vol. 30, no. 1, pp. 40–60, Jan. 2013.
- [32] P. Yang, Y. Xiao, B. Zhang, S. Li, M. El-Hajjar, and L. Hanzo, "Star-QAM signaling constellations for spatial modulation," *IEEE Trans. Veh. Technol.*, vol. 63, no. 8, pp. 3741–3749, Oct. 2014.
- [33] C. Pan, H. Ren, K. Wang, J. F. Kolb, M. El-kashlan, M. Chen, M. Di Renzo, Y. Hao, J. Wang, A. L. Swindlehurst, X. You, and L. Hanzo, "Reconfigurable intelligent surfaces for 6G systems: Principles, applications, and research directions," *IEEE Commun. Mag.*, vol. 59, no. 6, pp. 14–20, Jun. 2021.
- [34] L. You, J. Xiong, D. W. K. Ng, C. Yuen, W. Wang, and X. Gao, "Energy efficiency and spectral efficiency tradeoff in RIS-aided multiuser MIMO uplink transmission," *IEEE Trans. Signal Process.*, vol. 69, pp. 1407–1421, 2021.
- [35] C. You, B. Zheng, and R. Zhang, "Channel estimation and passive beamforming for intelligent reflecting surface: Discrete phase shift and progressive refinement," *IEEE J. Sel. Areas Commun.*, vol. 38, no. 11, pp. 2604–2620, Nov. 2020.
- [36] C. Pan, H. Ren, K. Wang, W. Xu, M. El-kashlan, A. Nallanathan, and L. Hanzo, "Multicell MIMO communications relying on intelligent reflecting surfaces," *IEEE Trans. Wireless Commun.*, vol. 19, no. 8, pp. 5218–5233, Aug. 2020.
- [37] C. Li, Y. Huang, M. Di Renzo, J. Wang, and Y. Cheng, "Low-complexity ML detection for spatial modulation MIMO with APSK constellation," *IEEE Trans. Veh. Technol.*, vol. 64, no. 9, pp. 4315–4321, Sep. 2015.
- [38] Q. Wu and R. Zhang, "Towards smart and reconfigurable environment: Intelligent reflecting surface aided wireless network," *IEEE Commun. Mag.*, vol. 58, no. 1, pp. 106–112, Jan. 2020.
- [39] J. G. Proakis and M. Salehi, *Digital Communications, 5th edition*. New York, NY, USA: McGraw-Hill, 2007.
- [40] A. M. Mathai and S. B. Provost, *Quadratic Forms in Random Variables: Theory and Applications*. New York: Marcel Dekker, 1992.
- [41] X. Dong, N. C. Beaulieu, and P. H. Wittke, "Error probabilities of two-dimensional M-ary signaling in fading," *IEEE Trans. Commun.*, vol. 47, no. 3, pp. 352–355, Mar. 1999.
- [42] Q. Wu and R. Zhang, "Beamforming optimization for intelligent reflecting surface with discrete phase shifts," in *Proc. IEEE ICASSP*, May 2019, pp. 7830–7833.
- [43] S. Zhang and R. Zhang, "Capacity characterization for intelligent reflecting surface aided MIMO communication," *IEEE J. Sel. Areas Commun.*, vol. 38, no. 8, pp. 1823–1838, Aug. 2020.

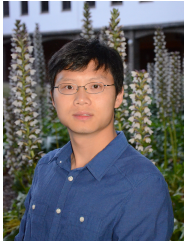


Mingjiang Wu is currently pursuing the Ph.D. degree with the School of Information Science and Technology, Southwest Jiaotong University, Chengdu, China. His current research interests include reconfigurable intelligent surface (RIS) and symbiotic radio (SR).



Xianfu Lei (Member, IEEE) received the Ph.D. degree from Southwest Jiaotong University in 2012. He has been an Associate Professor with the School of Information Science and Technology at Southwest Jiaotong University since 2015. From 2012 to 2014, he worked as a Research Fellow with the Department of Electrical and Computer Engineering at Utah State University. His research interests include 5G/6G networks, cooperative and energy harvesting networks, and physical-layer security. He currently serves as an Area Editor for IEEE COMMUNICATIONS LETTERS and as an Editor for IEEE TRANSACTIONS ON COMMUNICATIONS and IEEE WIRELESS COMMUNICATIONS LETTERS. He was Senior/Associate Editor for IEEE COMMUNICATIONS LETTERS from 2014-2019. He also served as symposium/track chairs for major IEEE conferences. He is a recipient of the Best Paper Award at IEEE/CIC ICC'20, the Best Paper Award at WCSP'18, the WCSP 10-Year Anniversary Excellent Paper Award, the IEEE Communications Letters Exemplary Editor Award, and the Natural Science Award of China Institute of Communications in 2019.

He is a recipient of the Best Paper Award at IEEE/CIC ICC'20, the Best Paper Award at WCSP'18, the WCSP 10-Year Anniversary Excellent Paper Award, the IEEE Communications Letters Exemplary Editor Award, and the Natural Science Award of China Institute of Communications in 2019.



Xiangyun Zhou (Senior Member, IEEE) is an Associate Professor at the Australian National University (ANU). He received the Ph.D. degree from ANU in 2010. His research interests are in the fields of communication theory and wireless networks. He has served as an Editor of IEEE TRANSACTIONS ON WIRELESS COMMUNICATIONS and IEEE WIRELESS COMMUNICATIONS LETTERS, and as an Area Editor of IEEE COMMUNICATIONS LETTERS. He also served as symposium/track and workshop chairs for major IEEE conferences. He was the chair of the ACT Chapter of the IEEE Communications Society and Signal Processing Society from 2013 to 2014. He is a recipient of the Best Paper Award at ICC'11 and IEEE ComSoc Asia-Pacific Outstanding Paper Award in 2016. He was named the Best Young Researcher in the Asia-Pacific Region in 2017 by IEEE ComSoc Asia-Pacific Board.

He was the chair of the ACT Chapter of the IEEE Communications Society and Signal Processing Society from 2013 to 2014. He is a recipient of the Best Paper Award at ICC'11 and IEEE ComSoc Asia-Pacific Outstanding Paper Award in 2016. He was named the Best Young Researcher in the Asia-Pacific Region in 2017 by IEEE ComSoc Asia-Pacific Board.



Yue Xiao (Member, IEEE) received the Ph.D degree in communication and information systems from the University of Electronic Science and Technology of China (UESTC) in 2007. He is currently a Professor with National Key Laboratory of Science and Technology on Communications, UESTC. He has published more than 100 international journals and has been in charge of more than 20 projects in the area of Chinese 3G/4G/5G wireless communication systems. He is an inventor of more than 50 Chinese and PCT patents on wireless systems. His research

interests are in system design and signal processing toward future wireless communication systems. He currently serves as a Senior Editor of IEEE COMMUNICATIONS LETTERS and an Associate Editor of IEEE Open Journal of the Communications Society.



Xiaohu Tang (Senior Member, IEEE) received the B.S. degree in applied mathematics from the Northwestern Polytechnical University, Xi'an, China, the M.S. degree in applied mathematics from the Sichuan University, Chengdu, China, and the Ph.D. degree in electronic engineering from the Southwest Jiaotong University, Chengdu, China, in 1992, 1995, and 2001 respectively.

From 2003 to 2004, he was a research associate in the Department of Electrical and Electronic Engineering, Hong Kong University of Science and Technology. From 2007 to 2008, he was a visiting professor at University of Ulm, Germany. Since 2001, he has been in the School of Information Science and Technology, Southwest Jiaotong University, where he is currently a professor. His research interests include coding theory, network security, distributed storage and information processing for big data.

Dr. Tang was the recipient of the National excellent Doctoral Dissertation award in 2003 (China), the Humboldt Research Fellowship in 2007 (Germany), and the Outstanding Young Scientist Award by NSFC in 2013 (China). He served as Associate Editors for several journals including IEEE TRANSACTIONS ON INFORMATION THEORY and IEEE TRANSACTIONS ON FUNDAMENTALS, and served on a number of technical program committees of conferences.



Rose Qingyang Hu (Fellow, IEEE) is a Professor in the Electrical and Computer Engineering Department and Associate Dean for research of College of Engineering at Utah State University. She also directs Communications Network Innovation Lab at Utah State University. Her current research interests include next-generation wireless system design and optimization, Mobile Edge Computing, V2X communications, artificial intelligence in wireless networks, wireless system modeling and performance analysis. Prof. Hu received the Ph.D. degree from the University of Kansas. Besides a decade academia experience, she has more than 10 years of R&D experience with Nortel, Blackberry, and Intel as a Technical Manager, a Senior Wireless System Architect, and a Senior Research Scientist, actively participating in industrial 3G/4G technology development, standardization, system level simulation, and performance evaluation. She has published over 270 papers in top IEEE journals and conferences and also holds numerous patents in her research areas. Prof. Hu is currently serving on the editorial boards of the IEEE TRANSACTIONS ON WIRELESS COMMUNICATIONS, the IEEE TRANSACTIONS ON VEHICULAR TECHNOLOGY, the IEEE WIRELESS COMMUNICATIONS. She also served as the TPC Co-Chair for the IEEE ICC 2018. She is IEEE Communications Society Distinguished Lecturer 2015-2018, IEEE Vehicular Technology Society Distinguished Lecturer 2020-2022, recipient of Best Paper Awards from the IEEE GLOBECOM 2012, the IEEE ICC 2015, the IEEE VTC Spring 2016, and the IEEE ICC 2016.

Prof. Hu received the Ph.D. degree from the University of Kansas. Besides a decade academia experience, she has more than 10 years of R&D experience with Nortel, Blackberry, and Intel as a Technical Manager, a Senior Wireless System Architect, and a Senior Research Scientist, actively participating in industrial 3G/4G technology development, standardization, system level simulation, and performance evaluation. She has published over 270 papers in top IEEE journals and conferences and also holds numerous patents in her research areas. Prof. Hu is currently serving on the editorial boards of the IEEE TRANSACTIONS ON WIRELESS COMMUNICATIONS, the IEEE TRANSACTIONS ON VEHICULAR TECHNOLOGY, the IEEE WIRELESS COMMUNICATIONS. She also served as the TPC Co-Chair for the IEEE ICC 2018. She is IEEE Communications Society Distinguished Lecturer 2015-2018, IEEE Vehicular Technology Society Distinguished Lecturer 2020-2022, recipient of Best Paper Awards from the IEEE GLOBECOM 2012, the IEEE ICC 2015, the IEEE VTC Spring 2016, and the IEEE ICC 2016.